rhodent: A python package for analyzing real-time TDDFT response

Computer Physics Communications 322 (2026) 110084

Contents lists available at ScienceDirect

Computer Physics Communications

journal homepage: www.elsevier.com/locate/cpc

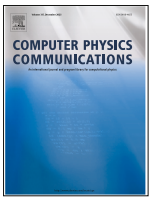

Computer Programs in Physics

rhodent: A python package for analyzing real-time TDDFT response

Jakub Fojt [a], Tuomas P. Rossi [b], Paul Erhart [a,*]

[a] Department of Physics, Chalmers University of Technology, 41296, Gothenburg, Sweden
[b] CSC - IT Center for Science Ltd, 405, 02101, Espoo, Finland

ARTICLE INFO

Editor: Prof. Blum Volker

Keywords:
Time-dependent density functional theory
Hot carrier
Nanoparticle
Plasmon

ABSTRACT

Real-time time-dependent density functional theory (rt-TDDFT) is a well-established method for studying the dynamic response of matter in the femtosecond or optical range. In this method, the Kohn-Sham (KS) wave functions are propagated forward in time, and in principle, one can extract any observable at any given time. Alternatively, by taking a Fourier transform, spectroscopic quantities can be extracted. There are many publicly available codes implementing rt-TDDFT, which differ in their numeric solution of the KS equations, their available exchange-correlation functionals, and in their analysis capabilities. For users of rt-TDDFT, this is an inconvenient situation because they may need to use a numerical method that is available in one code, but an analysis method available in another. Here, we introduce RHODENT, a modular Python package for processing the output of rt-TDDFT calculations. Our package can be used to calculate hot-carrier distributions, energies, induced densities, and dipole moments, and various decompositions thereof. In its current version, RHODENT handles calculation results from the GPAW code, but can readily be extended to support other rt-TDDFT codes. Additionally, under the assumption of linear response, RHODENT can be used to calculate the response to a narrow-band laser, from the response to a broad-band perturbation, greatly speeding up the analysis of frequency-dependent excitations. We demonstrate the capabilities of RHODENT via a set of examples, for systems consisting of Al and Ag clusters and organic molecules.

PROGRAM SUMMARY
Program Title: rhodent
CPC Library link to program files: https://doi.org/10.17632/ksp3gdsgw6.1
Developer's repository link: https://gitlab.com/materials-modeling/rhodent
Licensing provisions: MPL-2.0
Programming language: Python
Nature of problem: rt-TDDFT is a powerful method for probing the response of electronic systems. This method is implemented in several codes, with differing implementation details and possibilities for computing observables. However, if the full evolution of the density is recorded by the rt-TDDFT software, then it is possible to extract observables as a post-processing step. A modular implementation of the post-processing routines allows the same analysis to be applied to calculations performed using different rt-TDDFT programs. Furthermore, relatively weak perturbations are often of interest, so that the system response is in the linear regime. Then one single rt-TDDFT calculation with a broad-spectrum perturbation (e.g., a delta-kick) is enough to reconstruct the response for other perturbations (e.g., Gaussian laser pulses) in post-processing. Carrying out these post-processing steps is orders of magnitude faster than the rt-TDDFT calculation, and allows for computationally efficient analysis of the system at hand.
Solution method: We construct the Kohn-Sham density matrix using matrix operations, transform between the time and frequency domains by means of the discrete Fourier transform, and compute relevant observables by weighted summations. These operations are parallelized using the MPI library, allowing efficient execution on consumer-grade CPUs as well as on high-performance computer clusters.

* Corresponding author.
E-mail address: erhart@chalmers.se (P. Erhart).

https://doi.org/10.1016/j.cpc.2026.110084
Received 30 August 2025; Received in revised form 25 December 2025; Accepted 15 February 2026
Available online 16 February 2026

1. Introduction

Real-time time-dependent density functional theory (rt-TDDFT) is a well-established method for studying the response of electronic systems [1,2]. It has been used for spectroscopy calculations [3–10], including circular dichroism [11,12], X-rays [13], non-linear spectroscopy [14], and high-harmonic generation [15–17], as well as to study electron [18–23] and spin dynamics [24] on femtosecond timescales. In essence, one simply takes the ground state calculated with Kohn-Sham (KS)-density functional theory (DFT) [25,26] and numerically propagates the single-particle Schrödinger equation forward in time, under the influence of something driving the system out of the ground state, typically an external electric field. There are various codes implementing rt-TDDFT, including GPAW [27], OCTOPUS [28,29], TURBOMOLE [30], Siesta [31], CP2K [32], INQ [33], and QRCODE [34]. These codes differ in implementation details and numerical representations of the KS wave functions.

There is, however, a need for modular libraries [35]. It may be desirable for some users to employ one code, due to its numerical implementation details, while using the analysis capabilities of another. Without modular libraries, the only solution to this problem is for the developer to either port the analysis capabilities or the numerical implementation to the other code. Here, we introduce RHODENT – a Python package for processing the response from rt-TDDFT calculations. In its current version, calculation outputs from GPAW using the linear combination of atomic orbitals (LCAO) basis are supported, but the modular design of RHODENT prepares it for future integration with other programs. RHODENT is open source and comes with proper unit- and integration tests, easing development, even for external contributors. An extensive documentation is available online [36].

2. Program overview

The RHODENT package is written in Python and designed in a modular and object-oriented fashion. The key components are the `Response` and `Calculator` objects (Fig. 1). The `Response` class allows reading output files generated in a previous rt-TDDFT calculation (outside RHODENT), and transforms the response into the appropriate form for RHODENT, either in the time or frequency domain. There are several implemented `Response` classes, for use with different rt-TDDFT output files. The `Calculator` is responsible for computing the observables at various times in the simulation, or the Fourier transform thereof. Several `Calculator` classes are available.

The modular structure of RHODENT opens up the possibility to, with relatively little effort, extend the functionality of the code. In order to interface RHODENT to another rt-TDDFT code than GPAW, which is currently supported, a new `Response` class needs to be added. The new class should parse the appropriate output files, and iteratively return objects representing density matrices that are understood by the `Calculator` classes. We refer the interested reader to the online documentation [36] and source code repository of RHODENT to familiarize themselves with the internal structure of the code. Similarly, in order to compute a new type of observable, one in principle only needs to implement a new `Calculator`.

3. Implementation and theory

The central quantity that RHODENT works with is the time-dependent KS density matrix in the basis of ground-state KS orbitals

$$\rho_{nn'}(t) = \sum_k f_k \int \psi^*_{n'}(\boldsymbol{r},0)\psi_k(\boldsymbol{r},t)\mathrm{d}\boldsymbol{r} \int \psi^*_k(\boldsymbol{r}',t)\psi_n(\boldsymbol{r}',0)\mathrm{d}\boldsymbol{r}', \tag{1}$$

where $\psi_k(\boldsymbol{r},t)$ are the time-dependent KS wave functions and f_k their occupation numbers (including a spin degeneracy of 2). Here and in the following, k, n, and n' are indices enumerating the wave functions, or equivalently, the rows and columns of the KS density matrix. In particular, we are interested in the induced density matrix $\delta\rho_{nn'}(t) = \rho_{nn'}(t) - \rho_{nn'}(0)$. This quantity contains all information about the system response to some time-dependent perturbation $\hat{v}(t)$, and is obtained from an rt-TDDFT calculation (e.g., using GPAW). We note here that, since RHODENT currently is implemented for non-periodic and spin-paired systems, the only quantum number of the KS orbitals is n. We are restricted to fixed-atom calculations, so the time-dependence comes only from electronic degrees of freedom.

3.1. Obtaining the response

In RHODENT, we can work with the response in the time domain, which is obtained directly from the rt-TDDFT calculation, or in the frequency domain. For the latter, we define the normalized Fourier

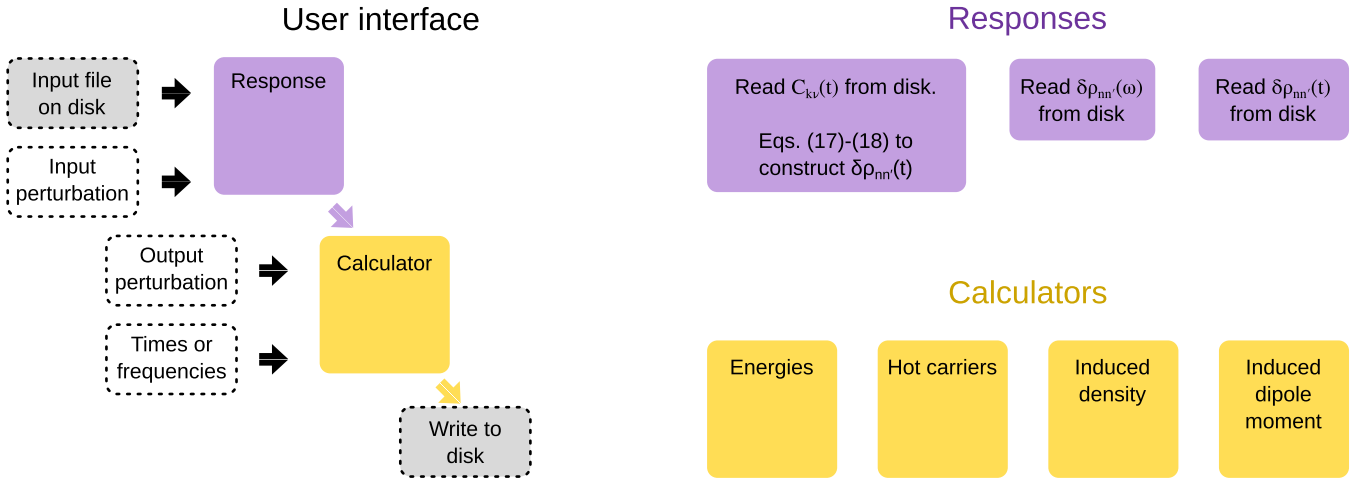

Fig. 1. Overview of the user interface for the RHODENT package. The RHODENT workflow consists of setting up a `Response` and a `Calculator` object, as shown by the arrows and boxes to the left in the figure. Input files (generated using rt-TDDFT) on disk are provided to the `Response` object, together with a description of the perturbation that generated the input files. An output perturbation and a set of times or frequencies are provided to the `Calculator` object. The `Calculator` object then transforms the input data appropriately to obtain the Fourier transform of the response at a given frequencies, or the response to the output perturbation at the given times. In the current implementation, there are three possible response types (shown in the upper right): reading time-dependent LCAO coefficients $C_{n\mu}(t)$ from disk, reading the Fourier transform of the induced KS density matrix $\delta\rho_{ia}(\omega)$ from disk, or reading the induced KS density matrix $\delta\rho_{ia}(t)$ from disk. There are four different calculators (lower right), calculating: energies, hot carriers, induced density and induced dipole moment.

transform

$$\frac{\delta\rho_{nn'}(\omega)}{v(\omega)} = \frac{\int_0^\infty \delta\rho_{nn'}(t)e^{i\omega t}\mathrm{d}t}{\int_0^\infty v(t)e^{i\omega t}\mathrm{d}t}, \tag{2}$$

where $v(t)$ is the scalar amplitude of the perturbation, and the lower bound on the integrals can be taken to be zero, because the integrands are zero before this time. This quantity is related to the Casida eigenvectors and gives similar information as the solution of the Casida equation [37].

3.1.1. In the frequency domain

In practice, the rt-TDDFT calculation results in samples of $\delta\rho(t)$ on a finite grid of N times $t_j = j\Delta t$. We then approximate $\delta\rho_{nn'}(\omega)$ by the discrete Fourier transform

$$\delta\rho_{nn'}(\omega) \approx \Delta t \sum_{j=0}^{N-1} \delta\rho_{ia}(t_j)e^{i\omega t_j}. \tag{3}$$

A common choice is to perform the rt-TDDFT calculation using a so-called δ-kick, where $v(t) = K\delta(t)$ and the Fourier transform $v(\omega) = K$ is exactly constant. For all other kinds of perturbations, we approximate

$$v(\omega) \approx \Delta t \sum_{j=0}^{N-1} v(t_j)e^{i\omega t_j}. \tag{4}$$

The finite simulation length results in a convolution of the true Fourier transform $\delta\rho_{nn'}(\omega)$ by a sinc-shape, leading to a noisy spectrum. A common remedy is to artificially dampen the response function, forcing it to zero before the end of the simulation. In RHODENT, Gaussian broadening is implemented, where the delta-kick response is multiplied by a Gaussian envelope of width σ

$$\delta\rho_{nn'}(\omega;\sigma) \approx \Delta t \sum_{j=0}^{N-1} \delta\rho_{ia}(t_j)e^{-\sigma^2 t_j^2/2}e^{i\omega t_j}. \tag{5}$$

This is equivalent to convoluting the noisy $\delta\rho_{ia}(\omega)$ with a Gaussian $e^{-\omega^2/2\sigma^2}$ in the frequency domain.

3.1.2. In the time domain through the convolution trick

The electron-hole part of the induced density matrix ρ_{ia}, where $f_i > f_a$ is linear in the perturbation [38], meaning that for sufficiently weak perturbations $\hat{v}$ there is a linear response regime where

$$\delta\rho_{ia}(t) = \int_0^t \hat{\chi}_{ia}(t-t')\hat{v}(t')\mathrm{d}t', \tag{6}$$

or equivalently, in the frequency domain,

$$\delta\rho_{ia}(\omega) = \hat{\chi}_{ia}(\omega)\hat{v}(\omega), \tag{7}$$

where $\hat{\chi}_{ia}$ is a response function describing the response of matrix element $\delta\rho_{ia}$ to $\hat{v}$. By convention, we use indices i and a to denote occupied and unoccupied ground state orbitals (equivalent to holes and electrons), respectively. Using RHODENT, we can exploit this linearity to compute the response $\delta\rho'_{ia}$ to perturbation $\hat{v}'$ knowing the response to $\delta\rho_{ia}$ to perturbation $\hat{v}$, without performing another rt-TDDFT calculation.

$$\delta\rho'_{ia}(\omega) = \hat{\chi}(\omega)\hat{v}'(\omega) \tag{8}$$

$$= \delta\rho_{ia}(\omega)\frac{v'(\omega)}{v(\omega)}. \tag{9}$$

We are restricted to perturbations of the same spatial shape, where the onset of $v'(t)$ is not earlier in time than $v(t)$, and where the spectrum of $v(\omega)$ covers $v'(\omega)$ entirely. The response in the time domain can be obtained by carrying out an inverse Fourier transformation of Eq. (9).

In practice, quantities are available on a finite grid of N times $t_j = j\Delta t$. We then take a discrete Fourier transform of the induced density matrix and both perturbations on the grid of N time instances

$$\delta\hat{\rho}_{k,ia} = \sum_{j=0}^{N-1} \delta\rho_{ia}(t_j)e^{i\omega_k t_j} \tag{10}$$

$$\hat{v}_k = \sum_{j=0}^{N-1} v(t_j)e^{i\omega_k t_j} \tag{11}$$

$$\hat{v}'_k = \sum_{j=0}^{N-1} v'(t_j)e^{i\omega_k t_j}. \tag{12}$$

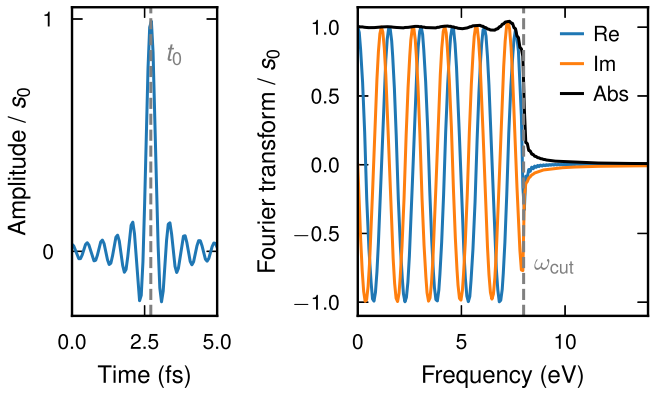

Fig. 2. Sinc-shaped pulse with cutoff $\hbar\omega_{\mathrm{cut}} = 8\,\mathrm{eV}$ and offset $t_0 = (5 + 1/4)/(2\pi\omega_{\mathrm{cut}})$ in the time and frequency domain. Choosing a multiple of an integer plus one quarter ensures that the pulse is finite at the beginning of the simulation.

Then $\hat{v}_k$ and $\hat{v}'_k$ are the kth Fourier components of the perturbations v and v', and $\delta\hat{\rho}_{k,ia}$ are the kth Fourier component of the ia matrix element of the induced KS density matrix. The chosen frequencies $\omega_k = 2\pi k/(\Delta t N')$ correspond to a grid of N' times (N' is at least $2N$), which is equivalent to padding the data with zeros after the end of the simulation. This is necessary to prevent circular correlation (see Appendix A). We obtain the induced density matrix to the new perturbation as the inverse discrete Fourier transform of Eq. (9)

$$\delta\rho'_{ia}(t_j) = \frac{1}{N'}\sum_{k=0}^{N-1}\frac{\delta\hat{\rho}_{k,ia}\cdot\hat{v}'_k}{\hat{v}_k}e^{-i\omega_k t_j}. \tag{13}$$

When constructing the density matrix from the time-dependent wave functions file, it is important to write the wave functions at every time step, if a δ-kick was used. Otherwise, if the wave functions are written at a sparse interval Δt there will be aliasing in the Fourier spectrum above the Nyquist frequency $1/2\Delta t$.

This behavior can be alleviated by using different temporal shapes. For example, a sinc-shaped pulse (Fig. 2)

$$v(t) = s_0\frac{\sin(\omega_{cut}(t-t_0))}{\omega_{cut}(t-t_0)}, t > 0 \tag{14}$$

has the Fourier transform

$$v(\omega) = s_0\frac{e^{i\omega t_0}}{\omega_{\mathrm{cut}}}\mathrm{rect}\left(\frac{\omega}{2\pi\omega_{\mathrm{cut}}}\right), \tag{15}$$

where the rectangular function $\mathrm{rect}(x)$ is equal to 1 for $0 < x < 1$ and 0 otherwise. In principle, this pulse does not induce any response above the cutoff frequency and allows saving the time-dependent wave functions file using a sparse interval.

However, in finite simulations, $v(\omega)$ is effectively convoluted with a sinc function leading to a smooth cutoff as $v(t)$ does not fit in the simulation window in its entirety. Choosing t_0, one should strike a balance between fitting as much as possible of $v(t)$ in the simulation window (leading to a sharper cut-off) and perturbing the system with a sufficiently strong field early on in the perturbation (leading to better numerical stability). In particular, it is a judicious choice to let the offset be an integer and a quarter offset of the time between oscillations $t_0 = (n + 1/4)/(2\pi\omega_{\mathrm{cut}})$ so that the pulse starts at a local maximum.

3.1.3. Constructing the KS density matrix

Currently, RHODENT provides an interface to the LCAO implementation of rt-TDDFT in GPAW [4,27,39]. In this implementation, the KS wave functions are represented as the linear combination

$$\psi_n(\boldsymbol{r},t) = \sum_\mu C_{n\mu}(t)\Phi_\mu(\boldsymbol{r}), \tag{16}$$

where $\Phi_\mu(\boldsymbol{r})$ are atom-centered orbitals (typically a few orbitals for each atom) and only the coefficients $C_{n\mu}$ are time-dependent. In the following, the Greek letters μ and ν enumerate the LCAO basis functions, or equivalently, the rows and columns of the density matrix in the LCAO basis.

3.1.4. Time-dependent wave functions file

In GPAW, the time-dependent coefficients $C_{n\mu}$ can be written to file periodically during time propagation. From this file, we can construct the KS density matrix in the LCAO basis

$$\rho_{\mu\nu}(t) = \sum_k C^*_{k\nu}(t) f_k C_{k\nu}(t). \tag{17}$$

Combining Eqs. (1) and (17), we find the basis transformation matrix $P_{n\mu} = \sum_\nu C_{n\mu}(0) S_{\nu\mu}$ with the overlap integral $S_{\mu\nu} = \int \Phi^*_\nu(\boldsymbol{r})\Phi_\mu(\boldsymbol{r})\mathrm{d}\boldsymbol{r}$. Then the induced density matrix in the basis of ground state KS orbitals is

$$\delta\rho_{nn'}(t) = \sum_{\mu\nu} P^*_{n'\nu}\left[\rho_{\mu\nu}(t) - \rho_{\mu\nu}(0)\right] P_{n\mu}. \tag{18}$$

3.1.5. Fourier transform of induced KS density matrix.

GPAW also supports building the Fourier transform $\delta\rho_{\mu\nu}(\omega) = \int_0^\infty [\rho_{\mu\nu}(t) - \rho_{\mu\nu}(0)] e^{i\omega t}\mathrm{d}t$ on the fly during time propagation on a grid of predefined frequencies [37]. Having saved this quantity to file, RHODENT can read it and transform the density matrix to the basis of ground state KS orbitals as

$$\rho_{nn'}(\omega) = \sum_{\mu\nu} P^*_{n'\nu}\rho_{\mu\nu}(\omega) P_{n\mu}. \tag{19}$$

3.1.6. Reading and writing numpy binary files

The construction of the density matrix from different sources, and transformations between time and frequency domain, are time and memory intensive (see Section 4.4). In particular, memory usage can be limiting in parallel execution as, for example, the transformation matrix $P_{n\mu}$ is duplicated on every process. Therefore, RHODENT allows writing the density matrix in the KS basis to a NumPy binary file on disk after every transformation. The files can be read in order to continue with another transformation (for example, the pulse convolution outlined in the next section), or simply to compute observables.

3.2. Calculating observables

In RHODENT `Calculators` are used to evaluate observables (yellow boxes in Fig. 1), which can be computed using the full response $\delta\rho_{ia}$, including:

- The density in the time domain, or the Fourier transform thereof.
- The dipole moment in the time domain, or its Fourier transform (the polarizability in the frequency domain).
- Stored energy in the system in the time domain.
- Electron and hole occupations, i.e., hot carrier (HC) distributions, in the time domain.

Additionally, a density of states calculator, which only relies on ground state information, and a spectrum calculator, which only needs a time-dependent dipole moment file, are implemented. For analysis purposes, the observables can be decomposed either by the energies or spatial confinement of occupied and unoccupied states i and a. For the latter, we use the Voronoi cell of an atom, which is the set of all points in space closer to that atom than to any other, to define the Voronoi weights

$$w^{\mathrm{proj}}_{nn'} = \int_{\text{Voronoi cell}} \psi^*_{n'}(\boldsymbol{r},0)\psi_n(\boldsymbol{r},0)\mathrm{d}\boldsymbol{r}. \tag{20}$$

In the following, we use Hartree atomic units.

Density

The induced charge density is obtained from $\delta\rho_{ia}$ as

$$\delta n(\boldsymbol{r}) = -\sum_{ia'} \psi^*_a(\boldsymbol{r},0)\psi_i(\boldsymbol{r},0)\delta\rho_{ia}. \tag{21}$$

Because the electron-electron and hole-hole parts of the KS density matrix ($\delta\rho_{nn'}$ where $f_n = f_{n'}$) are quadratic in perturbation, the electron-hole part dominates. Using that $\rho_{ia} = \rho^*_{ai}$ and that the KS orbitals are real, we can then write

$$\delta n(\boldsymbol{r}) = -2\sum_{ia}^{f_i>f_a} \psi_a(\boldsymbol{r},0)\psi_i(\boldsymbol{r},0)\mathrm{Re}\,\delta\rho_{ia}. \tag{22}$$

An energy filter can be supplied to RHODENT to include only a subset of transitions in the sum. For example, one could want to include only transitions to electrons above $\varepsilon_{\mathrm{low}}$ in energy

$$\delta n_{\mathrm{filter}}(\boldsymbol{r}) = -2\sum_{ia}^{\substack{f_i>f_a \\ \varepsilon_a>\varepsilon_{\mathrm{low}}}} \psi_a(\boldsymbol{r},0)\psi_i(\boldsymbol{r},0)\mathrm{Re}\,\delta\rho_{ia}. \tag{23}$$

Dipole moment

The induced dipole moment (dipole moment minus the static part) is

$$\delta\boldsymbol{\mu} = -2\sum_{ia}^{f_i>f_a} \boldsymbol{\mu}_{ia}\mathrm{Re}\,\delta\rho_{ia}, \tag{24}$$

where

$$\boldsymbol{\mu}_{ia} = \int \psi^*_a(\boldsymbol{r},0)\boldsymbol{r}\psi_i(\boldsymbol{r},0)\mathrm{d}\boldsymbol{r}. \tag{25}$$

We can use RHODENT to calculate the induced dipole Eq. (24), the induced dipole projected on Voronoi weights of occupied and unoccupied states for a projection on one or several atoms

$$\delta\boldsymbol{\mu}^{\mathrm{occ}\to\mathrm{unocc},ia} = -2\sum_{ia}^{f_i>f_a} \boldsymbol{\mu}_{ia}\mathrm{Re}\,\delta\rho_{ia} w^{\mathrm{proj,occ}}_{ii} w^{\mathrm{proj,unocc}}_{aa}, \tag{26}$$

or the dipole or projected dipole as a transition contribution map (TCM) [40]

$$-2\sum_{ia}^{f_i>f_a} \boldsymbol{\mu}_{ia}\mathrm{Re}\,\delta\rho_{ia} G(\varepsilon_{\mathrm{occ}} - \varepsilon_i) G(\varepsilon_{\mathrm{unocc}} - \varepsilon_a) \tag{27}$$

$$-2\sum_{ia}^{f_i>f_a} \boldsymbol{\mu}_{ia}\mathrm{Re}\,\delta\rho_{ia} w^{\mathrm{proj,occ}}_{ii} w^{\mathrm{proj,unocc}} G(\varepsilon_{\mathrm{occ}} - \varepsilon_i) G(\varepsilon_{\mathrm{unocc}} - \varepsilon_a). \tag{28}$$

The TCM enables illustrative analyses of matrices in the basis of ground state KS orbitals, by broadening them onto energy axes using Gaussians

$$G(\varepsilon - \varepsilon_n) = \frac{1}{\sqrt{2\pi\sigma^2}} \exp\left(-\frac{(\varepsilon - \varepsilon_n)^2}{2\sigma^2}\right). \tag{29}$$

For a perturbation corresponding to a spatially constant electric field polarized in the x direction

$$\hat{v}(t) = v(t)x, \tag{30}$$

the normalized Fourier transform of the induced dipole moment gives one column of the polarizability

$$\boldsymbol{\alpha}_x(\omega) = \frac{\int_0^\infty \delta\boldsymbol{\mu}(t) e^{i\omega t}\mathrm{d}t}{v(\omega)}. \tag{31}$$

In order to construct the full polarizability tensor, three rt-TDDFT calculations with orthogonal polarization directions along x, y, and z are needed

$$\boldsymbol{\alpha}(\omega) = \begin{bmatrix}\boldsymbol{\alpha}_x(\omega) & \boldsymbol{\alpha}_y(\omega) & \boldsymbol{\alpha}_z(\omega)\end{bmatrix}. \tag{32}$$

The optical absorption spectrum, expressed as the oscillator strength function, is related to the polarizability as

$$S_x(\omega) = \frac{2\omega}{\pi}\mathrm{Im}\,\alpha_{xx}(\omega). \tag{33}$$

This quantity obeys the sum rule that its integral $\int_0^\infty S(\omega)\mathrm{d}\omega$ equals the number of electrons in the system. The same kind of decomposition is available in the frequency domain as in the time domain. For example, we can construct the TCM [40] for the photoabsorption cross section

$$-\frac{4\omega}{\pi}\sum_{ia}^{f_i>f_a}\boldsymbol{\mu}_{ia}\frac{\mathrm{Im}\left[\mathrm{Re}\,\delta\rho_{ia}\right](\omega)}{v(\omega)}G(\varepsilon_{\mathrm{occ}}-\varepsilon_i)G(\varepsilon_{\mathrm{unocc}}-\varepsilon_a) \tag{34}$$

Stored energy

In KS DFT, the total energy E_{tot} can be partitioned into the kinetic energy T, the potential energy due to the Hartree and exchange-correlation (XC) potential E_{Hxc}, and the external energy. Using perturbation expansions up to second order [38] we can write the decomposition of the energy stored in the system

$$E_{\mathrm{tot}}(t) = E_{\mathrm{tot}}(0) + \delta T(t) + \delta E_{\mathrm{Hxc}}(t) + E_{\mathrm{field}}(t), \tag{35}$$

where the first term is the total energy of the ground state and the last term is the external energy due to the electric field of the perturbation

$$E_{\mathrm{field}}(t) = -\delta\boldsymbol{\mu}(t)\cdot\hat{\boldsymbol{e}}v(t). \tag{36}$$

Here, we assume that the electric field of the perturbation is spatially constant and polarized in $\hat{\boldsymbol{e}}$ direction. The change in kinetic and Hartree-exchange-correlation (Hxc) energies can be decomposed into contributions from all electron-hole transitions

$$\delta T(t) + \delta E_{\mathrm{Hxc}}(t) = \sum_{ia}^{f_i>f_a} E_{ia} \tag{37}$$

$$\delta E_{\mathrm{Hxc}}(t) = \sum_{ia}^{f_i>f_a} E_{ia}^{\mathrm{Hxc}}, \tag{38}$$

where

$$E_{ia} = \frac{1}{2}\left[p_{ia}\dot{q}_{ia} - q_{ia}\dot{p}_{ia} - v_{ia}q_{ia}\right] \tag{39}$$

$$E_{ia}^{\mathrm{Hxc}} = -\frac{1}{2}\left[\omega_{ia}q_{ia}^2 - q_{ia}\dot{p}_{ia} - v_{ia}q_{ia}\right] \tag{40}$$

are calculated from the following quantities and their time derivatives

$$p_{ia} = \frac{2\,\mathrm{Im}\,\delta\rho_{ia}}{\sqrt{2f_{ia}}} \tag{41}$$

$$q_{ia} = \frac{2\,\mathrm{Re}\,\delta\rho_{ia}}{\sqrt{2f_{ia}}} \tag{42}$$

$$f_{ia} = f_a - f_i \tag{43}$$

$$v_{ia} = \sqrt{2f_{ia}}\boldsymbol{\mu}_{ia}\cdot\hat{\boldsymbol{e}}v(t). \tag{44}$$

We can also calculate the rate of energy change using higher derivatives

$$\dot{E}_{ia} = \frac{1}{2}\left[p_{ia}\ddot{q}_{ia} - q_{ia}\ddot{p}_{ia} - v_{ia}\dot{q}_{ia} - \dot{v}_{ia}q_{ia}\right]. \tag{45}$$

For energies, we can compute Voronoi projections analogously to Eq. (26), and perform energy filtering based on the energy of pairs ia. For example, we can compute the total and Hxc energy above a threshold $\varepsilon_{\mathrm{low}}$

$$\delta E_{\mathrm{tot}}(t) = \sum_{ia}^{\substack{f_i>f_a \\ \varepsilon_a-\varepsilon_i>\varepsilon_{\mathrm{low}}}} E_{ia} \tag{46}$$

$$\delta E_{\mathrm{Hxc}}(t) = \sum_{ia}^{\substack{f_i>f_a \\ \varepsilon_a-\varepsilon_i>\varepsilon_{\mathrm{low}}}} E_{ia}^{\mathrm{Hxc}}. \tag{47}$$

Similarly, we can compute TCMs analogously to Eqs. (27) and (28).

Hot carriers

The equal-occupation-numbers part ($f_n = f_{n'}$) of the induced density matrix is quadratic in the perturbation [38], and can be obtained from the electron-hole part

$$\delta\rho_{nn'}(t) = \delta\rho_{nn'}^{\mathrm{electrons}}(t) - \delta\rho_{nn'}^{\mathrm{holes}}(t), \tag{48}$$

where

$$\delta\rho_{ii'}^{\mathrm{holes}} = \frac{1}{2}\sum_{a}^{f_i>f_a} p_{i'a}p_{ia} + q_{ia}q_{i'a} \tag{49}$$

$$\delta\rho_{aa'}^{\mathrm{electrons}} = \frac{1}{2}\sum_{i}^{f_i>f_a} p_{ia}p_{ia'} + q_{ia}q_{ia'}. \tag{50}$$

The purely electron-electron ($\delta\rho_{aa'}$, $f_a = f_{a'} = 2$) and hole-hole parts ($\delta\rho_{ii'}$, $f_i = f_{i'} = 0$) of the KS density matrix are equal to $\delta\rho_{aa'}^{\mathrm{electrons}}$ and $\delta\rho_{aa'}^{\mathrm{holes}}$, respectively, but for the partially occupied states $0 < f_n = f_{n'} < 2$ both terms in Eq. (48) are non-zero.

Hot-carrier distributions are calculated by convolution of $\delta\rho_{ii'}$ (holes) and $\delta\rho_{aa'}$ (electrons) with Gaussian broadening functions on the energy grid.

$$P^{\mathrm{holes}}(\varepsilon) = \sum_i \delta\rho_{ii}G(\varepsilon-\varepsilon_i) \tag{51}$$

$$P^{\mathrm{electrons}}(\varepsilon) = \sum_a \delta\rho_{aa}G(\varepsilon-\varepsilon_a). \tag{52}$$

We can also project hot-carrier distributions according to the Voronoi weights

$$P^{\mathrm{proj,holes}}(\varepsilon) = \sum_{ii'}\delta\rho_{ii'}w_{ii'}^{\mathrm{proj}}G(\varepsilon-\varepsilon_i) \tag{53}$$

$$P^{\mathrm{proj,electrons}}(\varepsilon) = \sum_{aa'}\delta\rho_{aa'}w_{aa'}^{\mathrm{proj}}G(\varepsilon-\varepsilon_a). \tag{54}$$

Optical spectrum and densities of state

Optical response calculations are a routine task in rt-TDDFT since the calculations by Yabana and Bertsch [3]. For spectroscopic applications, the dipolar response of the matter system due to a dipolar external field is of interest, as it is the only non-vanishing contribution in the far field.

$$\boldsymbol{d}(\omega) = \boldsymbol{\alpha}(\omega)\boldsymbol{E}_{\mathrm{ext}}(\omega), \tag{55}$$

or, equivalently, in the time domain

$$\boldsymbol{d}(t) = \int_0^t \boldsymbol{\alpha}(t-t')\boldsymbol{E}_{\mathrm{ext}}(t')\mathrm{d}t'. \tag{56}$$

Finally, we can compute the total density of states (DOS)

$$\sum_k G(\varepsilon-\varepsilon_k) \tag{57}$$

and the projected density of states (PDOS) as

$$\sum_k G(\varepsilon-\varepsilon_k)w_{kk}^{\mathrm{proj}}, \tag{58}$$

where w_{kk}^{proj} are the Voronoi weights given by Eq. (20).

4. Examples

In this section, we study three plasmonic systems to demonstrate the capabilities of RHODENT. The calculation workflow is as follows: For each system, we first compute the electronic ground state within DFT using LCAO basis sets in GPAW. Then we perform an rt-TDDFT calculation using GPAW, propagating the ground state in time under an external perturbation. We simulate the dynamics for 30 fs, which is enough to resolve the formation and subsequent dephasing of the localized surface plasmon resonance (LSPR). A propagation time step of 10 as yields converged results. We apply a sufficiently weak perturbation to only probe the linear-response domain. By choosing a sinc-shaped (Eq. (14)) perturbation in the time domain, we avoid exciting high frequency components of the response, which allows us to write a wave function trajectory to file at a relatively sparse interval, without risking aliasing. This file is read by RHODENT to calculate the response. Further information concerning the DFT and rt-TDDFT calculations can be found in Section 6. It should be emphasized here, that, while some of the calculations here (e.g., TCMs of induced dipoles) are already implemented as standard

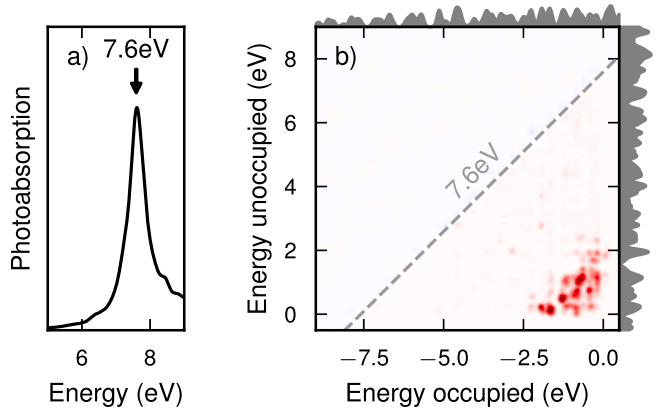

Fig. 3. (a) Absorption spectrum of the Al NP. (b) Transition contribution map (TCM) for the absorption of the Al NP at the frequency $\hbar\omega = 7.6\,\text{eV}$ (indicated in panel (a)). The color scale goes from white (no contribution) to red (positive contribution), and the DOS (Eq. (57)) is drawn on the outside of both energy axes. Energies are given with respect to the Fermi level. The diagonal line is drawn over resonant electron-hole transitions, i.e., those with an energy difference equal to $\hbar\omega$. There are no significant contributions to photoabsorption from resonant transitions. Instead, the main contributions are from transitions near the Fermi level. (For interpretation of the references to colour in this figure legend, the reader is referred to the web version of this article.)

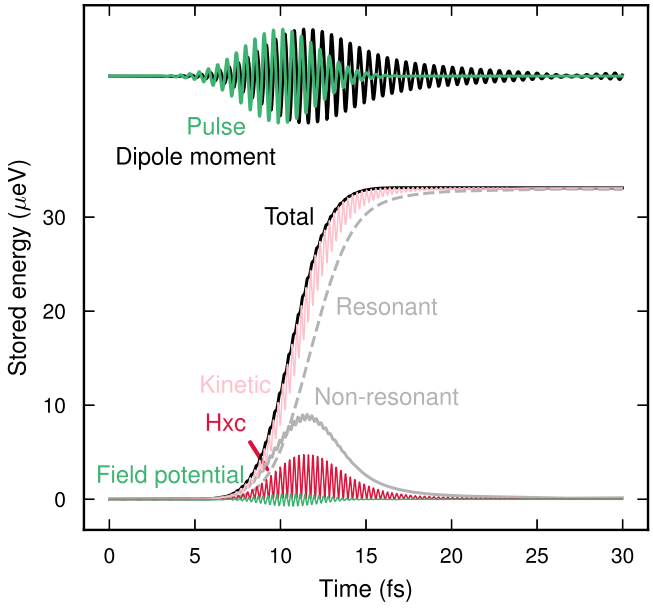

Fig. 4. Time-evolution of energy stored in the Al NP excited by a laser pulse resonant to the LSPR. The total energy is decomposed into Hxc contributions and kinetic contributions. An alternative decomposition is into energy of resonant and non-resonant transitions. The potential energy due to the external electric field (not included in the total), the pulse, and the induced dipole moment are also plotted in the figure.

features in GPAW, others are not (e.g., energies and HCs)). Even for the former case, RHODENT provides an advantage over the built-in GPAW implementation in its ease of use. At the same time, RHODENT gives the user the flexibility to perform pulse convolution in memory, and read from different types of output files.

4.1. Aluminum nanoparticle

As an initial example, we consider a plasmonic 201-atom Al nanoparticle (NP), with a diameter of 1.6 nm. An in-depth analysis of this system can be found in Ref. [10]. We perform one rt-TDDFT calculation, using a sinc-pulse with a cutoff of 16 eV, and write the wave function trajectory to disk at an interval of 100 as (Nyquist frequency of 20.7 eV). Due to the symmetry of the NP, its response is isotropic, and one polarization direction is enough to probe the entire response.

Analysis in the frequency domain

Using the dipole moment file from the rt-TDDFT calculation, and Eq. (33), we construct a photoabsorption spectrum (Fig. 3a) for the system. The main feature in the spectrum is a peak at 7.6 eV. We attribute the peak to the LSPR, which is a collective electronic excitation [41,42]. We can gain insight about the microscopic origin of this feature by constructing the TCM to the absorption, according to Eq. (34). This calculation requires the full response of the system, i.e., the wave function trajectory. Visualizing the contributions as a TCM (Fig. 3b), we see that many individual electron-hole pairs near the Fermi level collectively contribute to the absorption. We also compute the DOS, using Eq. (57), and plot it together with the TCM. Despite the energy difference between most involved electron and hole states being less than 3 to 4 eV or so, they are excited at 7.6 eV, thanks to their collective coupling through Coulomb interactions.

Analysis in the time domain

Now we consider the response of the Al NP to a Gaussian laser pulse. We consider a spatially constant electric field

$$\boldsymbol{E}_{\text{pulse}}(t) = \boldsymbol{E}_0 \cos(\omega_0(t - t_0)) \exp(-(t - t_0)^2/\tau^2), \tag{59}$$

choosing the strength $|\boldsymbol{E}_0| = 51\,\mu\text{V/Å}$, an envelope centered at $t_0 = 10\,\text{fs}$, and $\tau = 2.19\,\text{fs}$, giving a full width at half-maximum (FWHM) of about 5.2 fs in the time domain and 0.7 eV in the frequency domain. Thanks to the pulse convolution functionality in RHODENT (see Section 3.1.2), we do not need to perform any new rt-TDDFT calculations, which is the most expensive part of the simulation workflow. By appropriately setting up the `Response` object, the pulse convolution is performed before calculating observables.

We excite the system at the LSPR ($\hbar\omega_0 = 7.6\,\text{eV}$), and evaluate the time-dependence of the energy stored in the system (Fig. 4). As the pulse is turned on, the system responds with a dipole moment μ that lags roughly $\pi/2$ in phase after the electric field, corresponding to resonant response (absorption), and peaks in amplitude a few oscillations after the maximum of the pulse. Therefore, the energy contribution associated with the pulse (Eq. (36)) oscillates around zero at twice the pulse frequency.

The total energy increases during the entire duration of the pulse until it reaches a steady value. Having access to the full response, we can partition the total energy into kinetic and Hxc contributions, $\delta T(t)$ and $\delta E_{\text{Hxc}}(t)$, see Eqs. (37) and (38). We can see how energy is periodically redistributed between the former and the latter, at a frequency matching the pulse. Increasingly more energy is stored in kinetic contributions, while the amount of Hxc energy periodically reaches zero. The Hxc contributions persist for a few fs after the disappearance of the pulse, so we interpret this as the lifetime of the LSPR. Alternatively, we can partition the total energy into resonant and non-resonant contributions, by the distinction that the eigenvalue difference of resonant electron-hole pairs should be $|\hbar\omega_{ia} - \hbar\omega_0| < 1.4\,\text{eV}$. This tells us that the number of non-resonant transitions rises and falls smoothly, with only small oscillations, during the lifetime of the LSPR.

For even deeper insight into the data, we can construct TCMs for the energy contributions at selected times (Fig. 5). At the time instance marked (1) in Fig. 5a, when the Hxc contributions are at a maximum, we see both resonant and non-resonant transitions in the total energy (Fig. 5b), and only non-resonant transitions in the Hxc contribution (Fig. 5c). After one pulse cycle, at time instance (2), there are no Hxc contributions, but the same non-resonant transitions persist in the total energy (Fig. 5d). We should note here that these are the same transitions that are visible in the absorption TCM (Fig. 3b). It is now clear

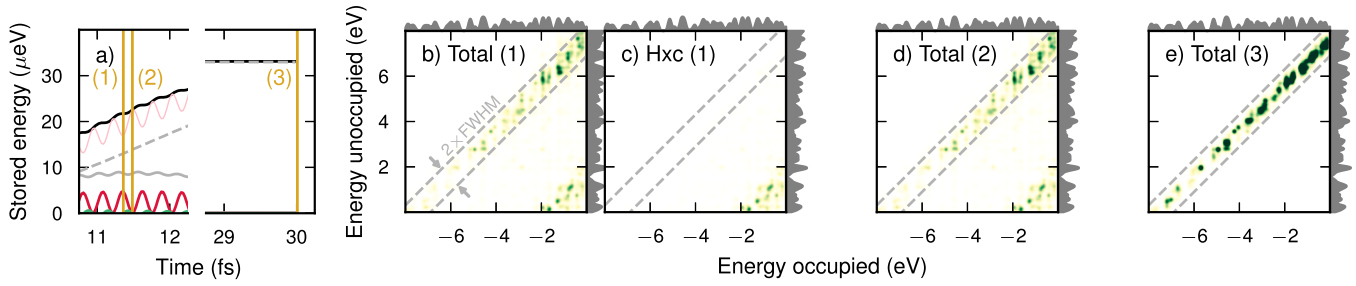

Fig. 5. (a) Time-evolution of energy stored in the Al NP excited by a laser pulse resonant to the LSPR, with time instances (1), (2) and (3) marked. (b) TCM of total and of (c) Hxc contributions at time instance (1). (d) TCM of total stored energy at time instance (2). (e) TCM of total stored energy at time instance (3). The transitions counted as resonant are indicated by dashed lines in (b-e). The same color scale, going from white (0) to green (positive), is used in all TCM axes, and the DOS is drawn outside each energy axis. (For interpretation of the references to colour in this figure legend, the reader is referred to the web version of this article.)

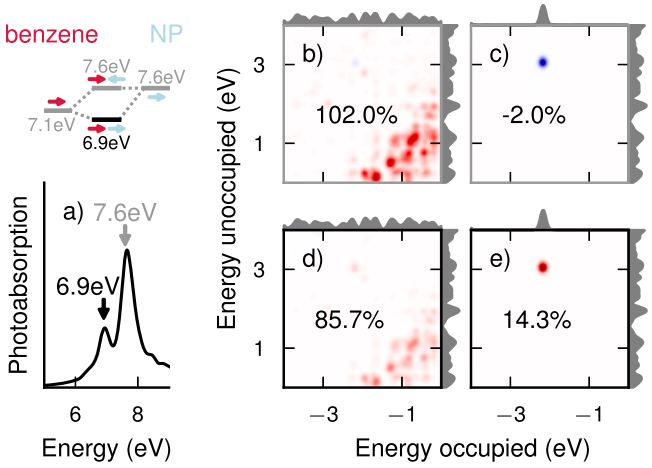

Fig. 6. (a) Absorption spectrum of the Al NP and benzene system. (b-e) TCMs for the absorption, for subset of transitions: (b) to the NP, at the UP frequency 7.6 eV, (c) to the molecule, at the UP frequency 7.6 eV, (d) to the NP, at the LP frequency 6.9 eV, (e) to the molecule, at the LP frequency 6.9 eV. For each of (b–e), the sum of the subset of transitions is written out as a fraction of the sum of all transitions at the same frequency. The same color scale, going from blue (negative) through white (0) to green (positive), is used in all TCM axes. The DOS is drawn outside each energy unoccupied energies axis, and the PDOS (for the NP or the molecule, as appropriate) is drawn outside each occupied energies axis. (For interpretation of the references to colour in this figure legend, the reader is referred to the web version of this article.)

that these transitions make up the LSPR, and that they oscillate between kinetic and potential energy during its lifetime. After the decay of the pulse, the plasmon dephases into resonant transitions, known as HCs. At time instance (3) only such transitions remain (Fig. 5e).

4.2. Aluminum nanoparticle with benzene molecules

The next example system is another structure from Ref. [10], made up of an Al NP identical to the previous structure, and two benzene molecules. The molecules are placed on opposite sides at a distance of 3 Å from the faces of the NP. The molecules are oriented such that the line through the molecules and the NP is parallel with the transition dipoles of the lowest bright excitations of the molecules. The system is no longer isotropic, so we constrain our analysis to excitation polarized along this axis. We perform a new rt-TDDFT calculation, with the same parameters as for the bare Al NP.

Analysis in the frequency domain

We calculate the photoabsorption spectrum (Fig. 6a), and find two peaks. One peak at 7.6 eV is very similar to the LSPR peak of the bare Al NP, but the other at 6.9 eV is both much larger in prominence and redshifted by about 0.2 eV compared to the peak of the bare molecules. This is a characteristic of strong coupling, where the underlying excitations (LSPR of the NP and the molecular excitation) exchange energy with each other at a faster or comparable rate to the lifetime of the excitations [43]. The two resonances are known as the lower polariton (LP) and the upper polariton (UP).

We decompose the absorption TCMs into NP-like and molecular transitions, using the Voronoi decomposition Eq. (26). In particular, we attribute transitions from occupied NP-states into any unoccupied state as the former, and transitions from occupied molecular states to any unoccupied state as the latter, because unoccupied states tend to be more of mixed character compared to occupied states. In Fig. 6b–e, we plot the projected TCMs together with the DOS (Eq. (57)) on the unoccupied energy axes, and the PDOS (Eq. (58)) for the NP/molecule on the occupied energy axes. At the UP frequency $\hbar\omega_0 = 7.6\,\text{eV}$, we find that the NP decomposition of the TCM (Fig. 6b) consists of the same excitations near the Fermi level that we attributed to the LSPR in the bare Al NP. Meanwhile, the molecular decomposition of the TCM (Fig. 6c) consists of a single excitation from the benzene highest occupied molecular orbital (HOMO) to the lowest unoccupied molecular orbital (LUMO). The molecular transition is contributing destructively to the absorption at the frequency of the UP, meaning that the molecular dipole is directed opposite to the NP dipole. At the LP frequency $\hbar\omega_0 = 6.9\,\text{eV}$, the TCM also consists of plasmonic transitions in the NP decomposition (Fig. 6d) and the single molecular excitation in the molecular decomposition (Fig. 6e). The difference is that for the LP, the LSPR and molecular excitation couple constructively. A configuration where the dipoles are parallel intuitively leads to a lower energy. The LP has significant molecular character, as 14.3 % of the absorption comes from the molecular transition, while the UP is almost entirely LSPR-like (the destructive contribution of the molecule is only 2.0 %).

Analysis in the time domain

Now we consider the time evolution of the dipole moment and energies after excitation by a Gaussian laser pulse. We excite the system with a pulse covering both peaks, with parameters $\hbar\omega_0 = 7.25\,\text{eV}$, $t_0 = 5\,\text{fs}$, and $\tau = 1.10\,\text{fs}$ (giving a FWHM of about 2.6 fs in the time domain and 1.4 eV in the frequency domain). We decompose the energies and dipoles in the same way as for the earlier frequency domain analysis, and find that a strong oscillating dipole first forms in the NP, then in the molecules, and then in the NP again (Fig. 7). These are Rabi oscillations, with 2-3 fs in between the maxima. Oscillations in the Hxc energy are visible in the NP and molecules during the same times as oscillations in the dipole. After 20 fs of simulation time, only kinetic energy remains (in the form of HCs), with a 92.3/7.7 % division between the NP and molecules.

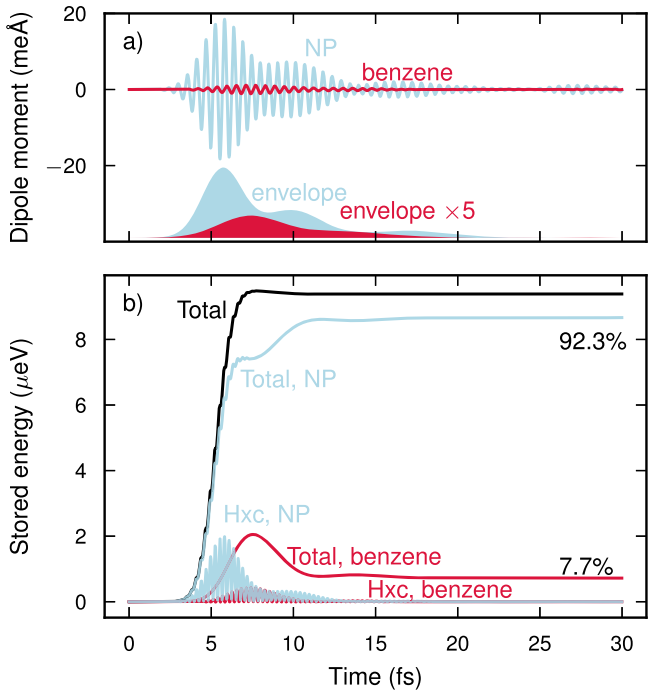

Fig. 7. For the Al NP and benzene molecule excited between the polaritons at frequency 7.25 eV, the time-evolution of (a) the induced dipole moment (decomposed into transitions to the NP and molecule) and (b) stored energy (decomposed into total/Hxc contributions and transitions to NP/molecule). The fraction of the total energy stored in the NP and molecule respectively, at the end of the simulation, are written out. The shaded areas in (a) show the envelopes of three/two Gaussians $Ae^{-(t-t_0)^2/2\tau^2}$ that have been fitted to the dipole moment of the NP/molecule.

4.3. Silver nanoparticle with CO molecule

As a final example, we consider a metal with valence d-electrons. We set up a 201-atom Ag NP (nearly the same diameter and shape as the Al NP), and place a CO molecule at a distance of 3 Å from the (111) on-top site. Detailed analysis of this system can be found in Ref. [23] We perform yet another rt-TDDFT calculation, with a polarization direction along the bond axis of the molecule. As for the Al systems, we use a time step of 10 as and a total simulation length of 30 fs. Because the relevant resonances are lower for this system compared to the Al NP, we use a sinc-pulse with a cutoff of 8 eV. This allows us to write the wave function trajectory to disk at an interval of 200 as (Nyquist frequency of 10.3 eV).

Analysis in the frequency domain

We calculate the photoabsorption spectrum (Fig. 8a) and identify the LSPR peak at 3.8 eV. Unlike the Al–benzene system we studied previously, the first bright excitation of the CO molecule (14.5 eV [23]) is far from the LSPR and its presence has a negligible effect on the absorption spectrum. We construct a TCM for the absorption spectrum (Fig. 8b) and see many excitations near the Fermi level constructively coupling at the LSPR frequency. A new feature, not found in the Al systems, are the destructive contributions involving transitions from the d-band edge (about 4 eV below the Fermi level) to unoccupied levels. These transitions are excited at the same time as the LSPR, with their dipoles opposite. Thus they screen the plasmon, contributing to a much lower resonance energy (3.8 eV) compared to the Al NP (7.6 eV).

Analysis in the time domain

Once again, we calculate the response to a Gaussian laser pulse. We choose the parameters $\hbar\omega_0 = 3.8$ eV, $t_0 = 10$ fs, and $\tau = 2.19$ fs (FWHM 7.3 fs in the time domain and 0.7 eV in the frequency domain) in order to cover the LSPR peak. For this system, we focus on the time after the dephasing of the plasmon. We compute the average of the hot hole (HH) and hot electron (HE) distributions (Fig. 9a) during the last 5 fs of the simulation, using Eqs. (51) and (52). We see that HCs are created in the NP, with energies spanning from 0 to the pulse frequency (or negative pulse frequency, for holes). As we saw in the energy TCM for the Al-system (Fig. 5e), HCs present after the dephasing of the plasmon are found on the diagonal $\varepsilon_a - \varepsilon_i = \hbar\omega_0$, where ε_a and ε_i are the energies of the electron and hole respectively. We also see this in that the HE distribution looks like the HH distribution, shifted upwards in energy by the pulse energy, except for some minor shifts due to the finite width of the pulse. At the Fermi level, there are both excited electrons and holes, due to the presence of partially occupied states in the ground state calculation.

For the Ag NP + CO molecule system, the molecular levels are hybridized with the metal states. The LUMO is split into several levels, around 1 to 2 eV above the Fermi level (Fig. 9b; top axes), while the HOMO is too far below the Fermi level to allow for excitations at the present pulse energy. Therefore, we can expect some HEs to form in the molecule but not any HHs. Indeed, computing the HC distribution

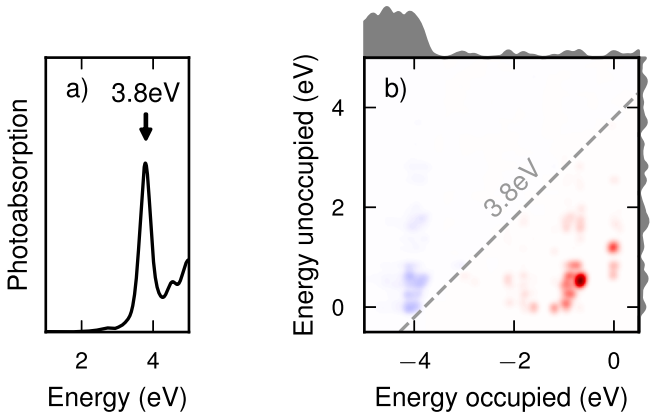

Fig. 8. (a) Absorption spectrum of the Ag NP and CO molecule. For this system, the molecule does not contribute to the absorption significantly. (b) Transition contribution map (TCM) for the absorption of the same system.

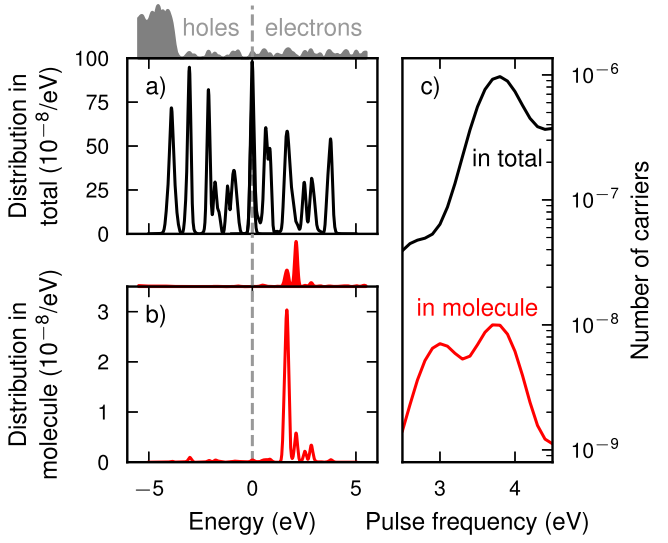

Fig. 9. (a) Hot-carrier distribution for the Ag NP + CO molecule system after excitation at resonance (3.8 eV). The DOS is drawn above the axes. (b) Hot-carrier distribution projected on the molecule after excitation at resonance (3.8 eV). The PDOS of the molecule is drawn above the axis. (c) The total number of excited electrons, and number of excited electrons in the molecule, as a function of excitation energy.

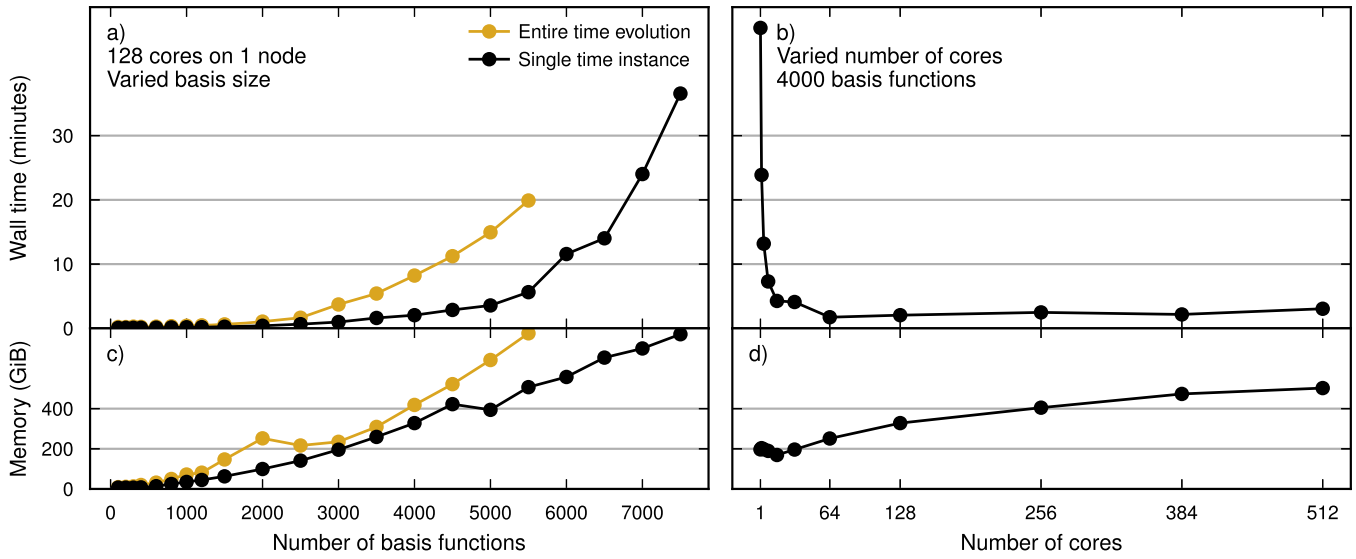

Fig. 10. Wall-time (a–b) and peak memory use (c–d) for two different benchmarks. In one benchmark, the entire time-evolution of the response was computed (yellow markers) while in the other the response at one time instance was computed (black markers). The benchmark tests were run on a system with dual AMD EPYC Zen2 2.25 GHz processors with 128 cores and 850GB available memory per node. In (a,c) the number of basis functions was varied using 128 cores on one node. In (b,d) the number of cores on one node (1 to 128 cores), two nodes (256 cores), three nodes (384 cores) and 4 nodes (512 cores) was varied for a system of 4000 basis functions. (For interpretation of the references to colour in this figure legend, the reader is referred to the web version of this article.)

projected on the molecule (Eqs. (53) and (54)) confirms that electrons are excited in the molecule in all branches of the hybridized LUMO (Fig. 9b). Interestingly, there is a delicate interplay between the coupling of each possible HC to the LSPR and the energetic alignment to the pulse that determines in which hybridized level most electrons are excited. This has been exploited in [23] to increase the amount of charge transfer.

Using RHODENT, we can, without much additional effort, compute the HC distributions for many different pulses at once. In Fig. 9c, we plot the total number of excited electrons in the system, as well as the number of excited electrons in the molecule, by pulse frequency. The total number of electrons is related to the amount of energy absorbed, which can be deduced from the absorption spectrum pulse frequency roughly like the absorption spectrum, as all the energy absorbed turns into HCs. For the number of electrons in the molecule, there are, however, several local maxima.

4.4. Performance analysis using synthetic data

Finally, we benchmark the performance of RHODENT. RHODENT is parallelized using the MPI library to distribute calculations over multiple processes. The implementation of the `Calculator` classes is comparatively simple compared to the `Response` classes. In the `Calculator` classes, calculations are trivially parallelized over time or frequency, with each MPI process working with the KS density matrix at either one time or frequency instance. While the user can decrease the wall-time of the calculation by distributing it over more MPI processes, this comes with an approximately linear increase in memory usage. The memory usage is predominantly determined by the size of all density matrices and output quantities that need to be concurrently held in memory.

In the `Response` classes, on the other hand, data is redistributed between the processes several times for more efficient calculations. The intermediate quantities needed to construct the response, as well as the overhead of MPI communication make it more difficult to know the memory usage beforehand. The interested reader is referred to the online documentation [36] and source code repository for details. For these reasons, we focus on the wall-time and memory usage of the calculation of the response from a time-dependent wave functions file, including the pulse convolution step (Eqs. (10)–(13)). A RHODENT workflow can always be split into one calculation of the response, writing the density matrices at desired times or frequencies to disk, and another calculation of the observables. The former is likely to become the bottleneck.

In the benchmark tests, we construct a synthetic dataset by generating a time-dependent wave functions file with random data for the LCAO coefficients $C_{n\mu}(t)$, and a corresponding file with basis transformation matrices $P_{n\mu}$ (see Eqs. (18)–(17)). The LCAO coefficients are represented numerically as N_{time} time instances t, N_{occupied} occupied KS states indexed by n and N_{basis} basis functions indexed by μ. We choose $N_{\text{time}} = 300$ (as in the example systems with Al), $N_{\text{occupied}} = N_{\text{basis}}/3$ (as is approximately the case for the basis sets used in the Ag example), and vary N_{basis}. With 16 bytes to store each complex coefficient, the size of the time-dependent wave functions file is thus 15 MB for $N_{\text{basis}} = 100$ and 84 GB for $N_{\text{basis}} = 7500$. We note that the Al example studied has $N_{\text{basis}} = 2829$ and that the Ag + CO example studied has $N_{\text{basis}} = 3635$.

We performed the benchmarks on a system with dual AMD EPYC Zen2 2.25 GHz processors with 128 cores and 850GB available memory per node. In one type of benchmark, we computed the entire time evolution of the induced KS density matrices and their first derivatives, as would be needed for, e.g., the calculation resulting in Fig. 4. In the other type of benchmark, we computed the induced KS density matrices and their first derivatives at one time instance only, as would be needed for, e.g., the calculation resulting in Fig. 9b–c. Performing the calculations on one node with 128 cores (Fig. 10a,c) and varying the system size N_{basis}, we see that the wall-time and peak memory use increases with $N_{\text{occupied}} \times N_{\text{basis}}$. In general, the wall-time of the calculations is a few to tens of minutes, and the peak memory usage is several times the size of the time-dependent wave functions file. In this test, RHODENT attempts to limit memory usage when reading the time-dependent wave functions file, which causes it to process the file in more chunks for the calculation of the entire time evolution, than for the calculation of a single time instance.

We also performed benchmarks (Fig. 10b,d) for a fixed system size of $N_{\text{basis}} = 4000$, varying the number of cores from 1 to 128 (on one node) and using 256, 384, or 512 cores on 2, 3, and 4 nodes. For this system, one observes that the optimal number of cores is around 64. When using fewer than 8 cores, the wall-time increases drastically (much more than the factor by which the number of cores is decreased), while the peak memory usage decreases only slightly. We have not investigated this

further, but a reasonable assumption is that the poor performance is related to poor utilization of the CPU cache. Using more than 64 cores, there is no improvement in wall-time for this system, which suggests that the overhead in distributing the data overshadows the speedup from having more processors working in parallel.

5. Conclusions and outlook

RHODENT is a Python package for post-processing the response of rt-TDDFT calculations. It can be used to obtain, e.g., induced dipole moments and densities, the stored energy, and HC distributions, as well as spatial and energetic projections thereof. Induced dipole moments and densities can also be computed in the frequency domain (the former being related to optical spectra). Additionally, since rt-TDDFT probes the linear response function when the external perturbation is sufficiently weak, RHODENT can quickly compute the response to any time-dependent perturbation in the linear response regime, from just one rt-TDDFT calculation. In the linear response regime, we can also exploit the structure of the density matrix to compute energies and HC distributions in the system.

Currently, RHODENT supports reading output files from GPAW calculations. The intention, however, is for RHODENT to be extensible and adaptable to a wider range of applications, including support for other rt-TDDFT packages. To this end, RHODENT has been designed with a modular structure and a clear separation between the construction of response and the computation of observables. Future development areas, ordered by presumed development cost, include, e.g., dense representations of wave functions, unpaired spins (e.g., to study spin-forbidden excitations or magnetism), and periodic boundary conditions (e.g., to study electron dynamics in surfaces or bulk materials).

RHODENT currently only allows parsing wave functions in the LCAO basis, as opposed to dense representations such as on uniform grids or using plane waves, since this representation is small and convenient to work with. Typically, the number of basis functions N_{basis} is a few times the number of occupied electrons in the system N_{occupied}. Then, the KS density matrix in the basis of all states (occupied and unoccupied) is of dimension $N_{\text{basis}} \times N_{\text{basis}}$. In a dense representation, N_{basis}, will typically be thousands of times larger than N_{occupied}, resulting in a much larger density matrix $N_{\text{basis}} \times N_{\text{basis}}$. Allowing such representations is thus a matter of finding a robust way to truncate them. A particular appealing approach could be to transform from the initial basis to maximally localized Wannier functions [44]. Such a representation would be sparse and thus retain the benefits of the LCAO basis already implemented in RHODENT in terms of computational efficiency and physical transparency.

In order to allow unpaired spins in RHODENT, the relations in Section 3 need to be derived under this condition (for reference, the derivations of the equations above can be found in Ref.[38]), and the implementation in RHODENT must be amended accordingly. A similar approach can be taken for extended systems. In this case, the polarizability Eq. (31) would be replaced by a susceptibility or dielectric function. One must work in the velocity instead of the length gauge in, e.g., Eq. (36) and the momentum degree of freedom of the response needs to be considered. Such extensions would expand the application range of RHODENT but also require substantial further development.

6. Computational details

The open-source GPAW [27] code package was used for the DFT and rt-TDDFT calculations. The calculations were done in the projector augmented wave (PAW) [45] formalism using LCAO basis sets [39]; the *pvalence* [4] basis set, which is optimized to represent bound unoccupied states, was used for the Ag species, and the double-zeta polarized (dzp) basis set for all other species. The PBE [46,47] (for the Al and Al + benzene calculations) and Gritsenko-van Leeuwen-van Lenthe-Baerends-solid-correlation (GLLB-sc) [48,49] (for the Ag + CO calculations) XC-functionals, utilizing the Libxc [50] library, were used in GPAW. For the Al and Al + benzene calculations, a simulation cell of $28.8\,\text{Å} \times 28.8\,\text{Å} \times 43.2\,\text{Å}$ was used. For the Ag + CO calculations, a simulation cell of $32.0\,\text{Å} \times 32.0\,\text{Å} \times 35.2\,\text{Å}$ was used. In the simulation cell, wave functions were represented with a grid spacing of $0.2\,\text{Å}$, and XC and Coulomb potentials with a grid spacing of $0.1\,\text{Å}$. Additional analytic moment corrections [51] centered at the NP were added to the Coulomb potential. Fermi-Dirac occupation number smearing with width $0.05\,\text{eV}$ was used. The self-consistent loop was stopped when the integral of the difference between two subsequent densities was less than 1×10^{-12}. Pulay [52]-mixing was used to accelerate the ground state convergence.

CRediT authorship contribution statement

Jakub Fojt: Writing – review & editing, Writing – original draft, Visualization, Software, Methodology, Investigation, Formal analysis, Data curation, Conceptualization; **Tuomas P. Rossi:** Writing – review & editing, Supervision, Software, Methodology, Investigation, Formal analysis, Data curation, Conceptualization; **Paul Erhart:** Writing – review & editing, Supervision, Software, Resources, Project administration, Methodology, Funding acquisition, Formal analysis, Conceptualization.

Data availability

The data generated for the examples in this article is available on Zenodo at https://doi.org/10.5281/zenodo.16746428. The RHODENT releases are accessible on Zenodo at https://doi.org/10.5281/zenodo.13332634 while the documentation can be accessed at https://rhodent.materialsmodeling.org.

Declaration of competing interest

The authors declare that they have no known competing financial interests or personal relationships that could have appeared to influence the work reported in this paper.

Acknowledgments

We acknowledge funding from the Knut and Alice Wallenberg foundation (Grant No. 2019.0140; J. F. and P. E.) and the Swedish Research Council (No. 2020-04935; J. F. and P. E.). The computations were enabled by resources provided by the National Academic Infrastructure for Supercomputing in Sweden (NAISS) at NSC, PDC and C3SE partially funded by the Swedish Research Council through grant agreement no. 2022-06725.

Appendix A. The convolution trick in finite simulations

In the linear response regime, we have that (dropping indices ia from the notation in the main text)

$$\delta\rho(t) = \int_0^t \chi(t')v(t-t')\mathrm{d}t', \tag{A.1}$$

where we assume that the perturbation $v(t)$ is zero before time zero, and the response is causal $\chi(t) = 0$ for $t < 0$. We can then work in the frequency domain

$$\delta\rho(\omega) = \chi(\omega)v(\omega), \tag{A.2}$$

where the Fourier transform is defined

$$\delta\rho(\omega) = \int_{-\infty}^{\infty} \delta\rho(t)e^{i\omega t}\mathrm{d}t, \tag{A.3}$$

and likewise for $\chi(\omega)$ and $v(\omega)$. As the Fourier transform is defined as an integration with infinite limits, and our simulations are finite, we need to reformulate the above relations in terms of finite integrations.

Here, we derive a frequency domain formula for quantities sampled in the time window $0 < t < T$.

First, we define the zero-padded quantity

$$v^{(0)}(t) = \begin{cases} v(t) & ,0 < t < T \\ 0 & ,T < t < T' \end{cases}, \tag{A.4}$$

which we take to be periodic with the period T'. Next, the crucial assumption is that T' is at least twice the length of T. Then, for $0 < t < T$, we can swap the perturbation by the zero-padded perturbation, and extend the limits of the convolution Appendix A.1

$$\delta\rho(t) = \int_0^T \chi(t')v^{(0)}(t-t')\mathrm{d}t'. \tag{A.5}$$

This holds because the added integral is zero

$$\int_t^T \chi(t') \underbrace{v^{(0)}(t-t')}_{=0} \mathrm{d}t' = 0. \tag{A.6}$$

We can now expand the zero-padded perturbation in a Fourier series of periodicity T'

$$v^{(0)}(t) = \frac{1}{T'}\sum_{k=-\infty}^{\infty} \hat{v}_k^{(0)} e^{-i\omega_k t}, \tag{A.7}$$

where $\omega_k = 2\pi k/T'$ and the Fourier coefficients

$$\hat{v}_k^{(0)} = \int_0^{T'} v^{(0)}(t)e^{i\omega_k t}\mathrm{d}t = \int_0^T v(t)e^{i\omega_k t}\mathrm{d}t \tag{A.8}$$

only require integration over the true perturbation in the window $0 < t < T$. Inserting the expansion of $v^{(0)}$ into Appendix A.5, we get

$$\delta\rho(t) = \frac{1}{T'}\sum_{k=-\infty}^{\infty} \hat{v}_k^{(0)} e^{-i\omega_k t}\int_0^T \chi(t')e^{i\omega_k t'}\mathrm{d}t' \tag{A.9}$$

$$= \frac{1}{T'}\sum_{k=-\infty}^{\infty} \hat{\chi}_k^{(0)}\hat{v}_k^{(0)} e^{-i\omega_k t}, \tag{A.10}$$

where we have defined the Fourier coefficients of the zero-padded response function

$$\hat{\chi}_k^{(0)} = \int_0^T \chi(t)e^{i\omega_k t}\mathrm{d}t. \tag{A.11}$$

We identify Appendix A.10 as a Fourier series for $\delta\rho(t)$, valid in the simulation time window $0 < t < T$, with the Fourier coefficients

$$\delta\hat{\rho}_k = \hat{\chi}_k^{(0)}\hat{v}_k^{(0)}. \tag{A.12}$$

These coefficients are not, in general, equal to the coefficients of the zero-padded induced density matrix

$$\delta\hat{\rho}_k^{(0)} = \int_0^T \delta\rho(t)e^{i\omega_k t}\mathrm{d}t, \tag{A.13}$$

but the Fourier series using $\delta\hat{\rho}_k$ and $\delta\hat{\rho}_k^{(0)}$ are equal inside the simulation window. The Fourier series Appendix A.10 is not, in general, zero outside the simulation time window $0 < t < T$.

Now, we consider a different pulse $v'(t)$ leading to a different response (new quantities denoted by primes)

$$\delta\rho'(t) = \int_0^t \chi(t')v'(t-t')\mathrm{d}t', \tag{A.14}$$

with Fourier coefficients defined

$$\hat{v}_k'^{(0)} = \int_0^T v'(t)e^{i\omega_k t}\mathrm{d}t, \tag{A.15}$$

and, as before, the Fourier coefficients $\delta\hat{\rho}'_k = \hat{\chi}_k^{(0)}\hat{v}_k'^{(0)}$ reproduce $\delta\rho'(t)$ in the simulation time window $0 < t < T$.

Now we require that the Fourier coefficients of the new pulse are non-zero for every non-zero coefficient of the old pulse, so that we can write

$$v_k'^{(0)} = K_k^{(0)} v_k^{(0)}, \tag{A.16}$$

which is equivalent (according to the circular correlation theorem) to the pulses being related by the convolution

$$v'^{(0)}(t) = \int_0^{T'} K^{(0)}(t')v^{(0)}(t-t')\mathrm{d}t', \tag{A.17}$$

where $K^{(0)}(t)$ is some zero-padded function and $K_k^{(0)}$ its Fourier coefficients. This means that the onset of the new pulse must be no later in time than the onset of the old pulse and introduce no new frequencies.

Then the Fourier series of the new response can be written

$$\delta\hat{\rho}'_k = \hat{\chi}_k^{(0)}K_k^{(0)}\hat{v}_k^{(0)} = K_k^{(0)}\delta\hat{\rho}_k, \tag{A.18}$$

which is also equivalent to a convolution with $K^{(0)}$. Because we are only interested in the response $\delta\rho'(t)$ during the simulation time $0 < t < T$, and $K^{(0)}$ is zero-padded, we can thus swap $\delta\hat{\rho}_k$ for $\delta\hat{\rho}_k^{(0)}$ and calculate the new response as the Fourier series

$$\delta\rho'(t) = \frac{1}{T'}\sum_{k=-\infty}^{\infty} \delta\hat{\rho}_k^{(0)}\frac{\hat{v}_k'^{(0)}}{\hat{v}_k^{(0)}}e^{-i\omega_k t}. \tag{A.19}$$

We have used that $K_k = \hat{v}_k'^{(0)}/\hat{v}_k^{(0)}$ for every non-zero value of $\hat{v}_k'^{(0)}$.

In practice, we have sampled $\delta\rho(t)$ and $v(t)$ on a grid of N times $t_j = j\Delta t$ with time step $\Delta t = T/N'$. Then the Fourier coefficients are approximated as

$$\delta\hat{\rho}_k = \Delta t\left(\sum_{j=0}^{N-1}\delta\rho(t_j)e^{i\omega_k t_j}\right) \tag{A.20}$$

and

$$\delta\rho^{(0)}(t_j) = \frac{1}{\Delta t}\left(\frac{1}{N'}\sum_{k=0}^{N'-1}\delta\hat{\rho}_k e^{-i\omega_k t_j}\right), \tag{A.21}$$

where the terms inside the brackets are the discrete Fourier transform and inverse discrete Fourier transform respectively, and $N' \geq 2N$. The approximation is good if the perturbation does not have any response above the Nyquist frequency $\omega = 2\pi/(2\Delta t)$; otherwise, aliasing effects are seen.

References

[1] M.R. Provorse, C.M. Isborn, Electron dynamics with real-time time-dependent density functional theory, Int. J. Quantum Chem. 116 (10) (2016) 739–749. https://doi.org/10.1002/qua.25096

[2] X. Li, N. Govind, C. Isborn, A.E.I. Deprince, K. Lopata, Real-time time-dependent electronic structure theory, Chem. Rev. 120 (18) (2020) 9951–9993. https://doi.org/10.1021/acs.chemrev.0c00223

[3] K. Yabana, G.F. Bertsch, Time-dependent local-density approximation in real time, Phys. Rev. B 54 (7) (1996) 4484–4487. https://doi.org/10.1103/PhysRevB.54.4484

[4] M. Kuisma, A. Sakko, T.P. Rossi, A.H. Larsen, J. Enkovaara, L. Lehtovaara, T.T. Rantala, Localized surface plasmon resonance in silver nanoparticles: atomistic first-principles time-dependent density-functional theory calculations, Phys. Rev. B 91 (11) (2015) 115431. https://doi.org/10.1103/PhysRevB.91.115431

[5] R. Sánchez-De-Armas, M.A. San-Miguel, J. Oviedo, A. Márquez, J.F. Sanz, Electronic structure and optical spectra of catechol on TiO 2 nanoparticles from real time TD-DFT simulations, Phys. Chem. Chem. Phys. 13 (4) (2011) 1506–1514. https://doi.org/10.1039/C0CP00906G

[6] P. Zhang, J. Feist, A. Rubio, P. García-González, F.J. García, Vidal, Ab initio nanoplasmonics: the impact of atomic structure, Phys. Rev. B 90 (16) (2014) 161407. https://doi.org/10.1103/PhysRevB.90.161407

[7] R. Sinha-Roy, P. García-González, H.-C. Weissker, F. Rabilloud, A.I. Fernández-Domínguez, Classical and ab initio plasmonics meet at sub-nanometric noble metal rods, ACS Photonics 4 (2017) 1484–1493. https://doi.org/10.1021/acsphotonics.7b00254

[8] J. Mattiat, S. Luber, Efficient calculation of (resonance) Raman spectra and excitation profiles with real-time propagation, J. Chem. Phys. 149 (17) (2018) 174108. https://doi.org/10.1063/1.5051250

[9] R.D. Senanayake, D.B. Lingerfelt, G.U. Kuda-Singappulige, X. Li, C.M. Aikens, Real-time TDDFT investigation of optical absorption in gold nanowires, J. Phys. Chem. C 123 (23) (2019) 14734–14745. https://doi.org/10.1021/acs.jpcc.9b00296

[10] T.P. Rossi, T. Shegai, P. Erhart, T.J. Antosiewicz, Strong plasmon-molecule coupling at the nanoscale revealed by first-principles modeling, Nat. Commun. 10 (1) (2019) 3336. https://doi.org/10.1038/s41467-019-11315-5

[11] K.-M. Lee, K. Yabana, G.F. Bertsch, Magnetic circular dichroism in real-time time-dependent density functional theory, J. Chem. Phys. 134 (14) (2011) 144106. https://doi.org/10.1063/1.3575587

[12] E. Makkonen, T.P. Rossi, A.H. Larsen, O. Lopez-Acevedo, P. Rinke, M. Kuisma, X. Chen, Real-time time-dependent density functional theory implementation of electronic circular dichroism applied to nanoscale metal-organic clusters, J. Chem. Phys. 154 (11) (2021) 114102. https://doi.org/10.1063/5.0038904

[13] J.M. Herbert, Y. Zhu, B. Alam, A.K. Ojha, Time-dependent density functional theory for X-ray absorption spectra: comparing the real-time approach to linear response, J. Chem. Theory Comput. 19 (19) (2023) 6745–6760. https://doi.org/10.1021/acs.jctc.3c00673

[14] Y. Takimoto, F.D. Vila, J.J. Rehr, Real-time time-dependent density functional theory approach for frequency-dependent nonlinear optical response in photonic molecules, J. Chem. Phys. 127 (15) (2007) 154114. https://doi.org/10.1063/1.2790014

[15] A. Castro, M.A.L. Marques, J.A. Alonso, G.F. Bertsch, A. Rubio, Excited states dynamics in time-dependent density functional theory, Eur. Phys. J. D At. Mol. Opt. Plasma Phys. 28 (2) (2004) 211–218. https://doi.org/10.1140/epjd/e2003-00306-3

[16] X. Chu, G.C. Groenenboom, Time-dependent density-functional-theory calculation of high-order-harmonic generation of H_2, Phys. Rev. A 85 (5) (2012) 053402. https://doi.org/10.1103/PhysRevA.85.053402

[17] F. Ding, B.E.V. Kuiken, B.E. Eichinger, X. Li, An efficient method for calculating dynamical hyperpolarizabilities using real-time time-dependent density functional theory, J. Chem. Phys. 138 (6) (2013) 064104. https://doi.org/10.1063/1.4790583

[18] S. Meng, E. Kaxiras, Electron and hole dynamics in dye-sensitized solar cells: influencing factors and systematic trends, Nano Lett. 10 (4) (2010) 1238–1247. https://doi.org/10.1021/nl100442e

[19] S.M. Falke, C.A. Rozzi, D. Brida, M. Maiuri, M. Amato, E. Sommer, A.D. Sio, A. Rubio, G. Cerullo, E. Molinari, C. Lienau, Coherent ultrafast charge transfer in an organic photovoltaic blend, Science 344 (6187) (2014) 1001–1005. https://doi.org/10.1126/science.1249771

[20] R. Long, O.V. Prezhdo, Instantaneous generation of charge-separated state on TiO2 surface sensitized with plasmonic nanoparticles, J. Am Chem. Soc. 136 (11) (2014) 4343–4354. https://doi.org/10.1021/ja5001592

[21] C. Lian, M. Guan, S. Hu, J. Zhang, S. Meng, Photoexcitation in solids: first-principles quantum simulations by real-time TDDFT, Adv. Theory Simul. 1 (8) (2018) 1800055. https://doi.org/10.1002/adts.201800055

[22] P.V. Kumar, T.P. Rossi, M. Kuisma, P. Erhart, D.J. Norris, Direct hot-carrier transfer in plasmonic catalysis, Faraday Discuss 214 (2019) 189–197. https://doi.org/10.1039/C8FD00154E

[23] J. Fojt, T.P. Rossi, M. Kuisma, P. Erhart, Hot-carrier transfer across a nanoparticle-molecule junction: the importance of orbital hybridization and level alignment, Nano Lett. 22 (21) (2022) 8786–8792. https://doi.org/10.1021/acs.nanolett.2c02327

[24] H. Li, Z. Pu, Y.Q. Gao, Y. Xiao, Real-time TDDFT using noncollinear functionals, J. Chem. Theory Comput. 20 (23) (2024) 10477–10490. https://doi.org/10.1021/acs.jctc.4c01218

[25] P. Hohenberg, W. Kohn, Inhomogeneous electron gas, Phys. Rev. 136 (3B) (1964) 864–B871. https://doi.org/10.1103/PhysRev.136.B864

[26] W. Kohn, L.J. Sham, Self-Consistent equations including exchange and correlation effects, Phys. Rev 140 (4A) (1965) 1133–A1138. https://doi.org/10.1103/PhysRev.140.A1133

[27] J.J. Mortensen, A.H. Larsen, M. Kuisma, A.V. Ivanov, A. Taghizadeh, A. Peterson, A. Haldar, A.O. Dohn, C. Schäfer, E.O. Jónsson, E.D. Hermes, F.A. Nilsson, G. Kastlunger, G. Levi, H. Jónsson, H. Häkkinen, J. Fojt, J. Kangsabanik, J.S. dequist, J. Lehtomäki, J. Heske, J. Enkovaara, K.T. Winther, M. Dulak, M.M. Melander, M. Ovesen, M. Louhivuori, M. Walter, M. Gjerding, O. Lopez-Acevedo, P. Erhart, R. Warmbier, R. Würdemann, S. Kaappa, S. Latini, T.M. Boland, T. Bligaard, T. Skovhus, T. Susi, T. Maxson, T. Rossi, X. Chen, Y.L.A. Schmerwitz, J.S. tz, T. Olsen, K.W. Jacobsen, K.S. Thygesen, GPAW: an open python package for electronic structure calculations, J. Chem. Phys. 160 (9) (2024) E92503. https://doi.org/10.1063/5.0182685

[28] N. Tancogne-Dejean, M.J.T. Oliveira, X. Andrade, H. Appel, C.H. Borca, G.L. Breton, F. Buchholz, A. Castro, S. Corni, A.A. Correa, U.D. Giovannini, A. Delgado, F.G. Eich, J. Flick, G. Gil, A. Gomez, N. Helbig, H. Hübener, R. Jestädt, J. Jornet-Somoza, A.H. Larsen, I.V. Lebedeva, M. Lüders, M.A.L. Marques, S.T. Ohlmann, S. Pipolo, M. Rampp, C.A. Rozzi, D.A. Strubbe, S.A. Sato, C. Schäfer, I. Theophilou, A. Welden, A. Rubio, Octopus, a computational framework for exploring light-driven phenomena and quantum dynamics in extended and finite systems, J. Chem. Phys. 152 (12) (2020) 124119. https://doi.org/10.1063/1.5142502

[29] A. Castro, M.A.L. Marques, A. Rubio, Propagators for the time-dependent Kohn-Sham equations, J. Chem. Phys. 121 (8) (2004) 3425–3433. https://doi.org/10.1063/1.1774980

[30] C. Müller, M. Sharma, M. Sierka, Real-time time-dependent density functional theory using density fitting and the continuous fast multipole method, J. Comput. Chem. 41 (30) (2020) 2573–2582. https://doi.org/10.1002/jcc.26412

[31] A. García, N. Papior, A. Akhtar, E. Artacho, V. Blum, E. Bosoni, P. Brandimarte, M. Brandbyge, J.I. Cerdá, F. Corsetti, R. Cuadrado, V. Dikan, J. Ferrer, J. Gale, P. García-Fernández, V.M. García-Suárez, S. García, G. Huhs, S. Illera, R. Korytár, P. Koval, I. Lebedeva, L. Lin, P. López-Tarifa, S.G. Mayo, S. Mohr, P. Ordejón, A. Postnikov, Y. Pouillon, M. Pruneda, R. Robles, D. Sánchez-Portal, J.M. Soler, R. Ullah, V.W.Z. Yu, J. Junquera, Siesta, Siesta: recent developments and applications, J. Chem. Phys. 152 (20) (2020) 204108. Recent developments and applications, https://doi.org/10.1063/5.0005077

[32] J. Hutter, M. Iannuzzi, F. Schiffmann, J. Vandevondele, CP2K: atomistic simulations of condensed matter systems, WIREs Comput. Mol. Sci. 4 (1) (2014) 15–25. https://doi.org/10.1002/wcms.1159

[33] X. Andrade, C.D. Pemmaraju, A. Kartsev, J. Xiao, A. Lindenberg, S. Rajpurohit, L.Z. Tan, T. Ogitsu, A.A. Correa, INQ , a modern GPU-accelerated computational framework for (time-dependent) density functional theory, J. Chem. Theory Comput. 17 (12) (2021) 7447–7467. https://doi.org/10.1021/acs.jctc.1c00562

[34] M. Choi, M.S. Okyay, A.P. Dieguez, M.D. Ben, K.Z. Ibrahim, B.M. Wong, QRCODE: massively parallelized real-time time-dependent density functional theory for periodic systems, Comput. Phys. Commun. 305 (2024) 109349. https://doi.org/10.1016/j.cpc.2024.109349

[35] S. Lehtola, A call to arms: making the case for more reusable libraries, J. Chem. Phys. 159 (18) (2023) 180901. https://doi.org/10.1063/5.0175165

[36] xxxx 2025.

[37] T.P. Rossi, M. Kuisma, M.J. Puska, R.M. Nieminen, P. Erhart, Kohn-Sham decomposition in real-time time-dependent density-functional theory: an efficient tool for analyzing plasmonic excitations, J. Chem. Theory Comput. 13 (10) (2017) 4779–4790. https://doi.org/10.1021/acs.jctc.7b00589

[38] T.P. Rossi, P. Erhart, M. Kuisma, Hot-carrier generation in plasmonic nanoparticles: the importance of atomic structure„ ACS Nano 14 (8) (2020) 9963–9971. https://doi.org/10.1021/acsnano.0c03004

[39] A.H. Larsen, M. Vanin, J.J. Mortensen, K.S. Thygesen, K.W. Jacobsen, Localized atomic basis set in the projector augmented wave method, Phys. Rev. B 80 (19) (2009) 195112. https://doi.org/10.1103/PhysRevB.80.195112

[40] S. Malola, L. Lehtovaara, J. Enkovaara, H. Häkkinen, Birth of the localized surface plasmon resonance in monolayer-protected gold nanoclusters„ ACS Nano 7 (11) (2013) 10263–10270. https://doi.org/10.1021/nn4046634

[41] C.F. Bohren, How can a particle absorb more than the light incident on it?, Am J. Phys. 51 (4) (1983) 323–327. https://doi.org/10.1119/1.13262

[42] E. Hutter, J.H. Fendler, Exploitation of localized surface plasmon resonance, Adv. Mater. 16 (19) (2004) 1685–1706. https://doi.org/10.1002/adma.200400271

[43] P. Törmä, W.L. Barnes, Strong coupling between surface plasmon polaritons and emitters: a review, Rep. Prog. Phys. 78 (1) (2014) 013901. https://doi.org/10.1088/0034-4885/78/1/013901

[44] N. Marzari, A.A. Mostofi, J.R. Yates, I. Souza, D. Vanderbilt, Maximally localized wannier functions: theory and applications, Rev. Mod. Phys. 84 (2012) 1419–1475. https://doi.org/10.1103/RevModPhys.84.1419

[45] P.E. Blöchl, Projector augmented-wave method, Phys. Rev. B 50 (24) (1994) 17953–17979. https://doi.org/10.1103/PhysRevB.50.17953

[46] J.P. Perdew, K. Burke, M. Ernzerhof, Generalized gradient approximation made simple, Phys. Rev. Lett. 77 (18) (1996) 3865. https://doi.org/10.1103/PhysRevLett.77.3865

[47] J.P. Perdew, K. Burke, M. Ernzerhof, Generalized gradient approximation made simple, Phys. Rev. Lett. 77 (7) (1996) 1396. Phys. Rev. Lett., https://doi.org/10.1103/PhysRevLett.78.1396

[48] O. Gritsenko, R.V. Leeuwen, E.V. Lenthe, E.J. Baerends, Self-consistent approximation to the Kohn-Sham exchange potential, Phys. Rev. A 51 (3) (1995) 1944. https://doi.org/10.1103/PhysRevA.51.1944

[49] M. Kuisma, J. Ojanen, J. Enkovaara, T.T. Rantala, Kohn-Sham potential with discontinuity for band gap materials, Phys. Rev. B 82 (11) (2010) 115106. https://doi.org/10.1103/PhysRevB.82.115106

[50] S. Lehtola, C. Steigemann, M.J.T. Oliveira, M.A.L. Marques, Recent developments in libxc - a comprehensive library of functionals for density functional theory, SoftwareX 7 (2018) 1–5. https://doi.org/10.1016/j.softx.2017.11.002

[51] A. Castro, A. Rubio, M.J. Stott, Solution of Poisson's equation for finite systems using plane-wave methods, Can. J. Phys. 81 (10) (2003) 1151–1164. https://doi.org/10.1139/p03-078

[52] P. Pulay, Convergence acceleration of iterative sequences. the case of scf iteration, Chem. Phys. Lett. 73 (2) (1980) 393–398. https://doi.org/10.1016/0009-2614(80)80396-4